# Accurate Maximum Power Tracking of Wireless Power Transfer System Based on Simulated Annealing Algorithm

**ZHONGZHENG LIN[1], JUNHUA WANG[1], ZHIJIAN FANG[1], MEILIN HU[1],
CHANGSONG CAI[1], AND JUNKUN ZHANG[2]**

[1]School of Electrical Engineering, Wuhan University, Wuhan 430072, China
[2]College of Electrical and Information Engineering, Hunan University, Changsha 410006, China

Corresponding author: Zhijian Fang (fzj@whu.edu.cn)

**ABSTRACT** Wireless power transfer (WPT) technology has become a popular solution to battery charging of mobile equipment. However, the variation of the load power will affect the transmission capacity of the system, which might make the electrical load cannot gain the required rated power and function improperly. Based on the analysis of power transmission characteristic and resonance state of WPT system, this paper adopts the simulated annealing (SA) method to track the maximum power point (MPP) of WPT in bifurcation state. The power tracking effectiveness of the proposed SA method is compared with that of the traditional maximum power point tracking method in WPT system based on perturbation and observation. The SA method performances under different parameters are assessed with consideration of the number of iterations needed for convergence and the convergence probability. Experimental validation of the maximum power tracking of WPT based on SA method is presented under different load conditions. Experimental results verify that the proposed SA method realizes the maximum power tracking when the WPT system works in the power bifurcation area, thus making full use of the inverter's VA capacity and approaching a unity power factor.

**INDEX TERMS** Maximum power transmission, wireless power transfer systems, simulated annealing, bifurcation.

## I. INTRODUCTION

Compared with the traditional wired charging method, the wireless power transfer (WPT) technology has the advantages of original physical isolation, protection from harsh environmental impact, convenience, and flexibility, so it can be widely applied in electric vehicles [1], [2], biomedical implants [3], and other fields [4]–[6]. The WPT system generates a rapidly changing magnetic field by applying high-frequency, high-current excitation to the transmitting coil. The induced voltage in receiving coil by the alternating magnetic field supplies power for the load in receiving side. However, the variation of the load and coupling coefficient between the coils will affect the transmission capacity of the system to some extent, which might make the load power less than the power rating and the WPT system cannot work normally [7], [8].

Therefore, in the design of WPT system, it is necessary to ensure the system to keep in resonance state to realize the maximum power transmission of the system, which is usually achieved through the control of the system's operating frequency or the system's resonance frequency. At present, the control methods to realize the maximum power transmission mainly include fixed frequency control and variable frequency control [9]. In fixed frequency control method, the maximum transmission capacity is obtained by changing resonance parameters of the WPT system through adjustable inductance or capacitance in series or parallel. Cheng Chen *et al.* have stabilized the output power by dynamically adjusting the compensating capacitance through variable shunt capacitance [10]. But the fixed frequency control method involves adding redundant tuning circuit and extra control to the tuning loop, which is sometimes difficult to apply in practice [11].

As for variable frequency control, it can be classified into phase feedback and power feedback according to different feedback variables.

Phase feedback method regulates the system transmission power by measuring the phase difference between the inverter output voltage and the output current. When the phase difference is 0°, the system reaches the full resonance state. Nan Liu *et al.* have measured the inverter output voltage and current through a series current sampling resistor and a parallel voltage sampling resistor [12]. The phase difference signal between the voltage and current was obtained after zero crossing detection and exclusive OR operation, and the optimal operating frequency was gained by adjusting the operating frequency to minimize the phase difference. Phase feedback method makes full use of the apparent capacity of the system and can make the system work in the area of the voltage phase slightly ahead, which is helpful to realize the zero-voltage switching operation. However, this method will lose the control stability due to the occurrence of multiple phase zero points of the system [13].

Power feedback method directly measures the active power of the system. The derivative of power to frequency is close to zero near the maximum power point (MPP). The slope of the power curve on the left of the maximum power point is greater than zero, and that on the right of the maximum power point is less than zero. The direction of frequency adjustment is obtained by calculating the derivative of power to frequency $dP/df$. Mohammad Ibrahim and others used this method to track the maximum power of an electric vehicle battery's wireless charging [14]. The phase difference between the AC voltage and current of the system is near zero, and the power transmission close to the unity power factor is realized.

In order to make the WPT system work stably in the maximum power transmission state in a large frequency range, the maximum power point tracking (MPPT) method is proposed based on the simulated annealing (SA) algorithm in this paper. This method iteratively searches for multiple power extremums of the WPT system in the bifurcation state so that the variable frequency control can operate in the bifurcation region. As the iteration proceeds, the final operating frequency will converge to the optimal operating point, so that the system remains maximum power transmission close to the unity power factor, avoiding the instability of the control in the case of bifurcation.

## II. MAXIMUM POWER TRANSMISSION AND RESONANCE STATE ANALYSIS OF WPT SYSTEM

The mutual inductance model of wireless power transfer system in which the primary side and the secondary side simultaneously adopt series compensation is given in figure 1. $R_1$ is the resistance value considering the connection between the internal resistance of the power supply and the internal AC resistance of the coil in series. $R_2$ is the equivalent load resistance merging with the internal AC resistance of the receiving coil. $L_1$, $L_2$, and $M$ is the self-inductance and
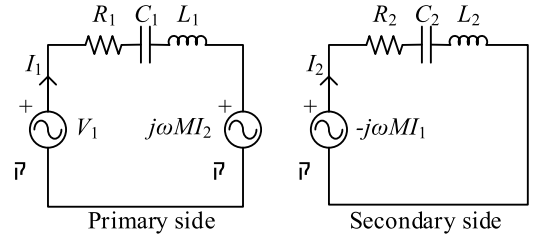


**FIGURE 1.** Mutual inductance model of the WPT system.

mutual inductance of coupling coils. $C_1$, $C_2$ are the series compensating capacitance, respectively.

It is necessary to make the system work in the area of zero input phase angle to get the input of the WPT system reach the unity power factor and make full use of the VA capacity of the system. When the reactive input power is zero, the series loop resonates, and the reactive power consumed by the inductor in the system is compensated by the reactive power generated by the capacitor.

To describe the maximum input power characteristics and the resonance characteristics of a series-series WPT system, two main parameters are introduced as shown in equation (1): the generalized detuning factor $\xi$ and the generalized coupling factor $\eta$ [15]:

$$\xi = \left( \frac{\omega}{\omega_0} - \frac{\omega_0}{\omega} \right) Q, \quad \eta = kQ$$

$$\xi = \frac{\omega L - 1/\omega C}{R}, \quad \eta = \frac{\omega M}{R}, \quad (1)$$

where $R$, $L$, $C$ are the resistors, inductors, and capacitors of the series circuit, $M$ is the mutual inductance between the coils, and $\omega_0$ is the natural resonance frequency of the LC loop, $\omega$ is the excitation frequency in radians, $k$ is the coupling coefficient between the coils, and $Q$ is the quality factor of the LC loop (related to $R$).

It can be seen that the definitions of $\xi$ and $\eta$ still have the meaning of expressing detuning and coupling after introducing the quality factor:

1. The definition of $\xi$ indicates the extent to which the LC resonant tank is affected by the excitation frequency offset. The higher the $Q$ value, the greater the influence of the detuning. When $\omega = \omega_0$, $\xi = 0$, it means that the LC circuit reaches resonance state.

2. The definition of $\eta$ indicates the degree to which the coupled circuit's primary side and the secondary side interact with each other. Both the increase of the quality factor $Q$ and that of the coupling coefficient $k$ will raise the generalized coupling factor $\eta$. At the same time, $\eta = kQ$ has also been discussed and analyzed in some articles of WPT [16]–[19].

After the introduction of the generalized detuning factor $\xi$ and the generalized coupling factor $\eta$, the impedance of the original system can also be expressed by multiplying the

primary and secondary sides' impedance:

$$
\begin{cases}
Z_1 = R_1 + j\omega L_1 - j\dfrac{1}{\omega C_1} \\
\quad = R_1(1 + j\xi_1) \\
Z_2 = R_2 + j\omega L_2 - j\dfrac{1}{\omega C_2} \\
\quad = R_2(1 + j\xi_2) \\
X_M = j\omega M \\
\quad = R_1\eta_1 = R_2\eta_2
\end{cases}
\tag{2}
$$

For the primary side and the secondary side, the subscript -1 and -2 distinguish respectively $(\xi_1, \xi_2, \eta_1, \eta_2)$. We assumed that $\xi_1 = \xi_2 = \xi$, $\eta_1 = \eta_2 = \eta$ to simplify the analysis, which can be achieved by using the same LC design as well as an appropriate impedance transformation for both sides. The impedance expressions (2) are brought into the original system's KVL equation, and the active input power and the input phase angle are obtained:

$$
\begin{cases}
P_1 = \dfrac{V_1^2}{R_1}\dfrac{(1+\xi^2)+\eta^2}{(1-\xi^2+\eta^2)^2 + 4\xi^2} \\
\angle\dfrac{V_1}{I_1} = \angle\left( R_1\dfrac{(1+j\xi)^2 + \eta^2}{(1+j\xi)} \right)
\end{cases}
\tag{3}
$$

After normalizing $V_1$ and $R_1$, the transmission power and input phase angle are illustrated in figure 2 and figure 3 with $\xi$ and $\eta$ as variables.
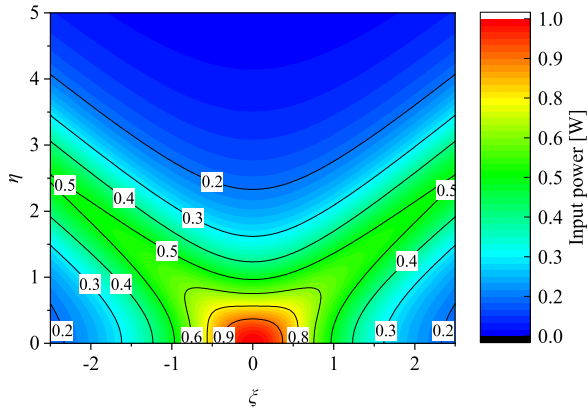


**FIGURE 2.** The contour map of input power characteristic.

From figure 2, it can be derived that the maximum input power is at

$$
\begin{cases}
\xi_{\text{PMAX}} = 0 \\
P_{1\max} = \dfrac{1}{1+\eta^2}
\end{cases}
\quad (\eta < 1/\sqrt{3}),
\tag{4}
$$

The maximum input power point begins to deviate from the point $\xi = 0$ as the generalized coupling factor $\eta$ gradually increases to $\eta > 1/\sqrt{3}$, and two new maximum power points appear in pairs on both sides of $\xi = 0$:

$$
\begin{cases}
\xi_{\text{PMAX}} = \pm\sqrt{2\eta\sqrt{\eta^2+1}-(\eta^2+1)} \\
P_{1\max} = \dfrac{1}{4}\dfrac{1}{\eta\sqrt{\eta^2+1}-\eta^2}
\end{cases}
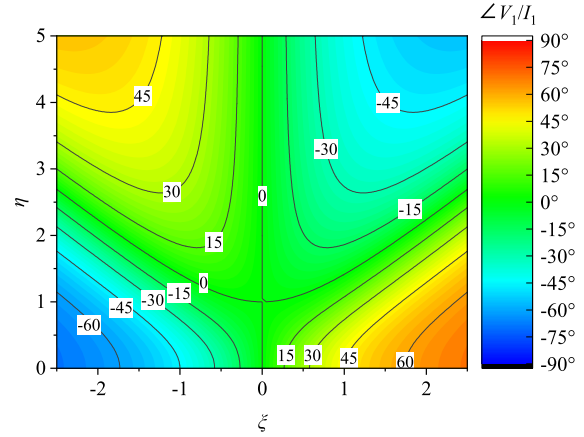\quad (\eta \geq 1/\sqrt{3})
\tag{5}
$$



**FIGURE 3.** The contour map of the input phase angle.

The active input power is also maximized at the new resonance point. The existence of a specific inverter frequency at $\xi > 0$ causes the primary impedance $Z_1$ and the secondary reflected impedance $Z_r$ to resonate in series.

Therefore, it is essential to adjust the operating frequency and $\xi$ to adapt to the change of the generalized coupling factor $\eta$ to reach maximum power transmission.

Figure 3 shows the phase difference between input voltage $V_1$ and input current $I_1$. When the voltage and current remain in phase, the input phase angle is zero, where the power factor is equal to 1, thereby minimizing the reactive power requirements of the WPT system. It can be seen from figure 3 that the zero point of input phase angle is split at $\eta = 1$, and the system obtains three zero input phase angles as $\eta$ continues to increase:

$$
\xi_{\angle 0} = 0, \quad \pm\sqrt{\eta^2 - 1}
\tag{6}
$$

The split trajectory of the zero phase angle divides the $\xi$-$\eta$ plane into four operating regions. The input current in the four regions presents a state of capacitive versus inductive distribution, that is, the unity power factor occurs under three conditions:

(1) The primary side's LC loop and the secondary side's LC loop are respectively resonant in series, corresponding to the resonance point $\xi_{\angle 0} = 0$.

(2) The primary impedance $Z_1$ presents inductive and the reflected impedance $Z_r$ acts as a capacitor, and a series resonance occurs between $Z_1$ and $Z_r$, corresponding to the resonance point $\xi_{\angle 0} = \sqrt{(\eta^2 - 1)}$.

(3) The primary impedance $Z_1$ presents capacitive and the reflected impedance $Z_r$ acts as an inductor, and a series resonance occurs between $Z_1$ and $Z_r$, corresponding to the resonance point $\xi_{\angle 0} = -\sqrt{(\eta^2 - 1)}$.

Based on the above analysis, it can be inferred that the maximum power input does not mean the full resonance of the WPT system, and their generalized detuning factor $\xi$ conditions are not entirely equivalent. However, it is important to note that the maximum power transmission condition and the unity power factor condition can be achieved at a similar

inverter operating frequency when $\eta \gg 1$, since $\xi_{\text{PMAX}} \approx \xi_{\angle 0} \approx \eta$. Therefore, by tracking the maximum input power, the WPT system can acquire unity power factor, operate at the maximum power point and make full use of the VA capacity.

## III. MAXIMUM POWER TRACKING BASED ON SIMULATED ANNEALING ALGORITHM

This paper considers transforming the maximum power point tracking (MPPT) problem into the optimization problem of searching for the maximum power value to adapt to the situation where multiple input power peaks may occur in a WPT system. That is, the maximum power of the system is achieved by searching for the optimal operating frequency, and the boundary conditions of the optimization problem are determined by the compensation topology and the limitation of the control frequency of the system. To avoid the influence of local maxima caused by splitting, the MPPT method in this paper is based on the simulated annealing (SA) algorithm. SA algorithm is a global optimization method based on the physical process of metal annealing, which has been applied to various optimization problems since its introduction [20]–[27].

However, SA algorithm has its own shortcoming, which is the accuracy of the solution of the optimal frequency and the efficiency of the algorithm are often not compatible. Increasing the accuracy of the frequency solution is often accompanied by a long iterative process. Conversely, improving the efficiency of the algorithm is often accompanied by a reduction in the quality of the solution. This is manifested by the algorithm's greater sensitivity to parameter settings.

Therefore, when using the SA method for maximum power point tracking design, we should focus on improving (1) the update strategy of frequency $f_{\text{next}}$, and (2) temperature decay scale $\alpha$, thus, achieving a compromise between frequency resolution accuracy and solution speed for more efficient applications.

(1) For the frequency update strategy, a larger frequency conversion range centered on the reference point means that the algorithm can search for the maximum power point faster. However, large frequency variations are detrimental to the inverter of the WPT system. Therefore, the range of frequency update in this paper is selected within $\pm 100$Hz of the reference operating point to ensure stable operation of the system.

(2) For the temperature decay process, it's important to control the speed of temperature decay. When the temperature decays slowly, the frequency tracking results are more accurate, but the iterative decay process also increases. When the temperature decays faster, the algorithm solves faster, but the accuracy of convergence will worsen.

The convergence characteristic of the SA algorithm depends on the settings of its annealing temperature including initial temperature, termination temperature, and temperature decay scale. At each temperature condition, the SA algorithm will perform several random perturbations near the reference point (operation frequency) and measure the corresponding input power. When the inverter of the WPT system is powered

by a stable DC bus voltage, only the input current on the DC bus is measured at the reference point. Then the perturbation current $i_{\text{next}}$ is compared with the reference current $i_{\text{pre}}$. If higher current is obtained at the perturbation frequency, then that frequency will be accepted as the new reference working point. On the contrary, if $i_{\text{next}}$ is lower than $i_{\text{pre}}$, that frequency can still be accepted as a reference point based on the acceptance probability $X$, and the acceptance probability $X$ is related to the current difference $\Delta i = i_{\text{next}} - i_{\text{pre}}$ and the annealing temperature $T$, which is expressed as:

$$X = e^{K\frac{\Delta i}{T}} \tag{7}$$

$\Delta i$ represents the difference between the perturbation current $i_{\text{next}}$ and the reference current $i_{\text{pre}}$. $K$ is the current magnification factor that adjusts the probability curve to ensure a uniform distribution of the curve. $T$ is the annealing temperature of the algorithm. The acceptance probability $X$'s profile is illustrated in figure 4.
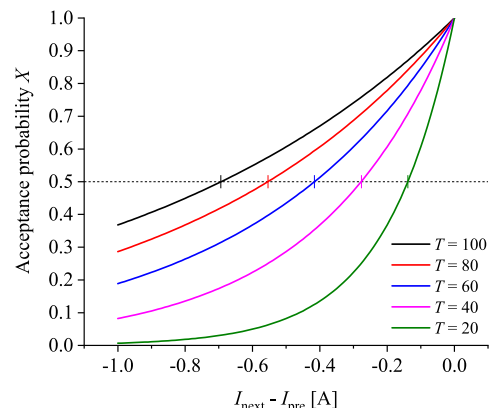
**FIGURE 4.** The relation of acceptance probability *X* to the current difference Δ*i* and temperature *T*.

As can be seen, when $T$ is high, or $|\Delta i|$ is small, the probability that the algorithm accepts a lower input current is high, and the algorithm is not affected by the local maximum. When $T$ gradually decreases or $|\Delta i|$ is large, the probability $X$ is relatively low, and the algorithm is more inclined to receive a larger current. For example, taking the probability greater than 0.5 as a condition of acceptance, when $T = 100$, the lowest acceptable operating point is 0.7 amperes lower than the reference current. With $T$ reducing, the $|\Delta i|$ acceptable is reduced to 0.15 amperes when $T = 20$.

The SA algorithm can accept a lower current as a reference point for the next perturbation, which allows the algorithm to cross some local power maximum points during higher temperature operation. As the temperature continues to decrease, the probability that a lower current perturbation point will be accepted is almost reduced to zero, and only a higher current perturbation point is accepted as a new reference, thus ensuring that the algorithm can converge to the global maximum power point after crossing the local maxima power points.
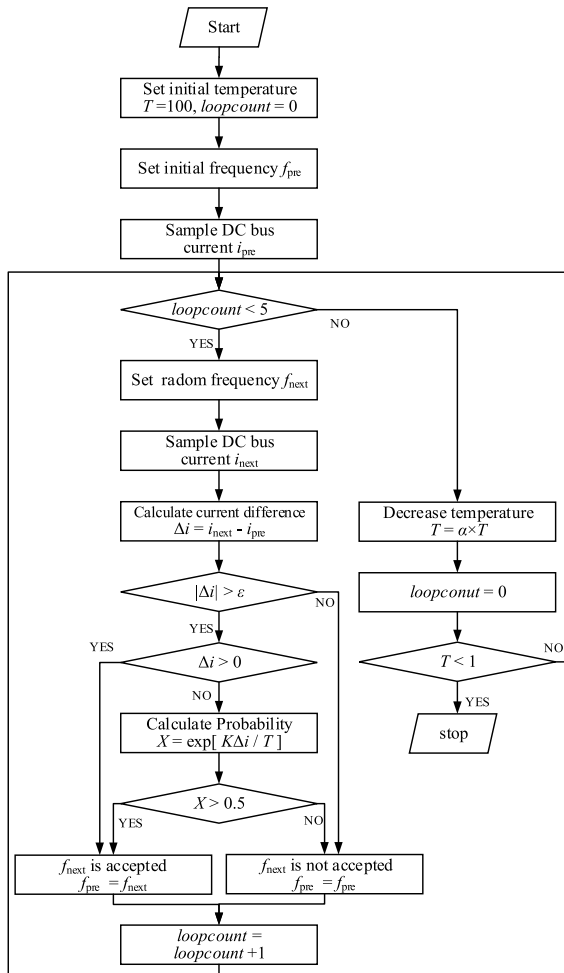
**FIGURE 5. MPPT method based on simulated annealing algorithm.**



**FIGURE 6. Diagram of MPPT control based on SA algorithm for WPT system.**

**TABLE 1. Experimental setup parameters.**

| Symbol | Quantity | Value |
|--------|----------|-------|
| $V_{in}$ | DC bus voltage | 24 V |
| $R_{AC}$ | Equivalent rectifier load | 5 Ω - 30 Ω |
| $L_P$ | Transmitting coil self-inductance | 92.4 μH |
| $R_P$ | Transmitting coil internal resistance | 0.49 Ω |
| $L_S$ | Receiving coil self-inductance | 88.9 μH |
| $R_S$ | Receiving coil internal resistance | 0.28 Ω |
| $M$ | Mutual inductance | 39.7 μH |
| $C_P$ | Primary compensation capacitor | 34.18 nF |
| $C_S$ | Secondary compensation capacitor | 34.21 nF |
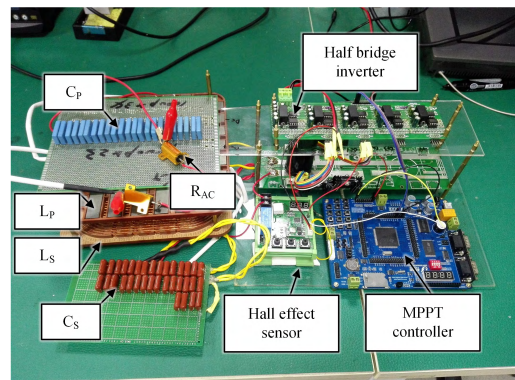


**FIGURE 7. Experimental system setup for MPPT implementation.**

Figure 5 is the flow chart of the MPPT method based on SA algorithm for a WPT system at a single temperature, where $i_{pre}$ and $i_{next}$ are reference and perturbation current values after sampling on the DC bus and filtering respectively. Since the DC bus voltage $V_{DC}$ is stable, the sampled current can reflect the input power of the system. $\varepsilon$ is set to a tiny positive number to reduce the error of current sampling and misoperation. $X$ is the acceptance probability of the SA algorithm to accept lower power as a reference point. Annealing temperature $T$ decreases with an iterative process. This paper uses an equal-scale decay process:

$$T(n) = \alpha T(n-1) \tag{8}$$

$\alpha$ is the decay scale of annealing temperature $T$, which is between 0 and 1. The bigger $\alpha$, the slower the temperature decay process.

## IV. PROTOTYPE IMPLEMENTATION

The WPT system constructed in this paper is given in figure 6, in which a DC voltage $V_{in}$ is used to supply for MOSFET half-bridge inverter. The primary and secondary sides are compensated in series with the film capacitors $C_P$, $C_S$ respective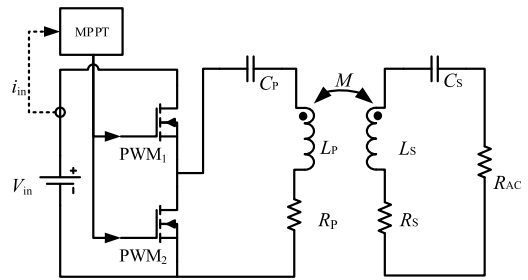ly. The transmitting coil $L_P$ and receiving coil $L_S$ are the litz wired coils with square spiral structure and a fixed spacing. The load of the WPT system is an aluminum shell resistor $R_{AC}$ equivalent to the general rectifier load. The measurement results of component parameters are shown in table 1. The MPPT controller collects the DC bus current through the Hall effect sensor, calculates the input power, and outputs the PWM signal to control the half-bridge inverter's operating frequency. The system setup is shown in figure 7.

To determine whether the system is in the bifurcation region, the operating frequency range of the system is considered according to the analysis of the resonance parameters. In this paper, the PWM signal period is from 6.7 μs to 20 μs (corresponding to PWM frequency 150 kHz - 50 kHz). After taking the component parameters in Table 1 into equation (1)

and taking the geometric mean of the primary and secondary sides' resonance parameters, we get $\xi = \sqrt{\xi 1 \xi 2}$ and $\eta = \sqrt{\eta 1 \eta 2}$. Taking the $\xi$ - $\eta$ plane of figure 2 as the resonance state space, the system working state coordinates $(\xi, \eta)$ under different $R_L$ are plotted on that $\xi - \eta$ plane, as shown in figure 8. It can be seen that the resonance state of the system shifts with the change of frequency, crossing two power peaks. Thus it can be inferred that the transmission power of the WPT system is in bifurcation state with the parameter setting in table 1.
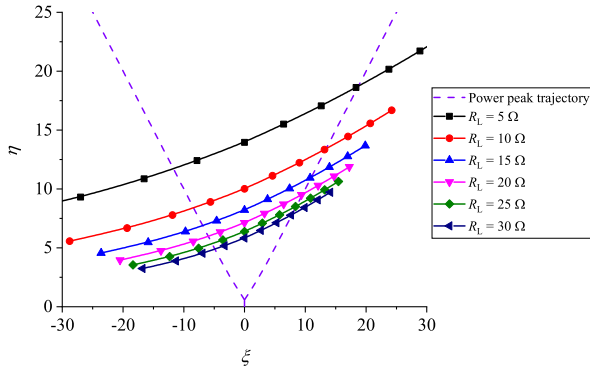


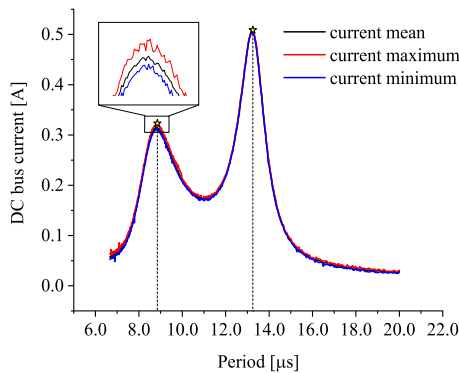**FIGURE 8.** The system resonance state varies with working frequency *f* and load *R*L.



**FIGURE 9.** Sample input current characteristics when *R*AC = 15 Ω.

Frequency scanning analysis of the input current is carried out, where the PWM signal period is from 6.7 $\mu$s to 20 $\mu$s (corresponding to PWM frequency 150 kHz - 50 kHz), and the relation between the input current and the period of the PWM signal is shown in figure 9.

The input current characteristic curve reveals its characteristic of having multiple power peaks at a constant bus voltage. As analyzed before, when the system is operating in the bifurcation region, there will be multiple power maximums. It can be seen that the system has a global peak of current at 13.2 $\mu$s of the PWM signal period (frequency = 73.5 kHz) and a local peak of current at period = 8.9 $\mu$s (frequency = 112.4 kHz).

On the other hand, the characteristic curve is not entirely smooth that the current fluctuates within a certain interval, which leads to a "band-like" distribution of input current characteristic. As a result of the measurement error of the
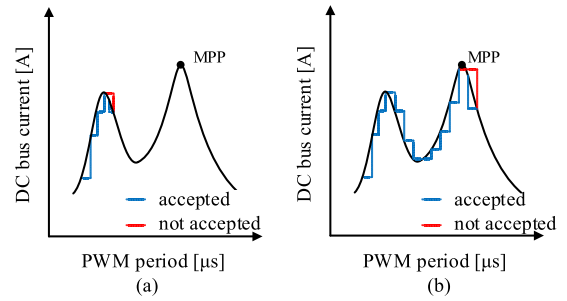


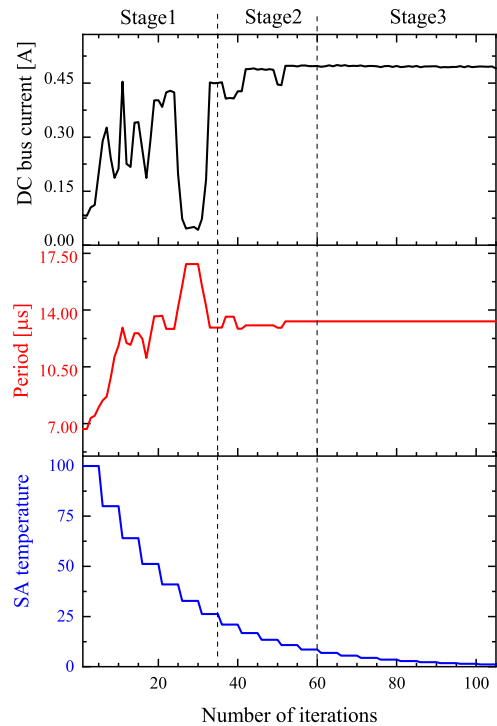**FIGURE 10.** The comparison of the convergence process between (a) the P&O method and (b) the SA method.



**FIGURE 11.** The convergence process of the implemented SA method when *R*AC =15 Ω.

current sensor, the measured current value will contain some noise mentioned above, thus resulting many random local current maximums in the frequency perturbation process.

If the system adopts the general perturbation and observation (P&O) method for maximum power point tracking [28], the tracking results will be affected by the local maximum point and many other random maximum points. Once the system falls into these maximum points, it means the failure of the control, as shown in figure 10.

The MPPT based on the SA algorithm is different from the general P&O method. It can accept low current values at the reference point, which means that the SA algorithm is not affected by the local maximum and converges to the global maximum.

The control process of the SA algorithm is shown in figure 11, and the parameter settings is shown in table 2.

As can be observed from figure 11, as the number of iterations increases, the operation frequency of the system

**TABLE 2.** Parameters of simulated annealing algorithm experiment.

| Symbol | Quantity | Value |
|--------|----------|-------|
| $T_0$ | The initial temperature | 100 |
| $T_n$ | The terminated temperature | 1 |
| $\alpha$ | The temperature decay scale | 0.8 |
| | The number of iterations at the same temperature | 5 |
| $\varepsilon$ | The current comparison threshold | 0.01 |
| $K$ | The current gain factor | 100 |
| | The range of PWM period | 6.7 µs - 20 µs |
| | The range of PWM frequency | 5 kHz - 150 kHz |
| | The range of $f_{next}$ | $f_{pre} \pm 100$Hz |

eventually converges to the maximum power operating point before the temperature drops to the termination temperature. The system obtains the maximum input power at this operating point. According to the above analysis, the VA capacity of the system is also fully utilized at this working point.

At the high-temperature iteration stage 1, the algorithm has a great probability of accepting a lower current perturbation points as the reference point for the next iteration. It is ensured that the algorithm will not be affected by the local maximum of power in the early period of the iteration so that it can continue to iterate in an extended frequency range.

At stage 2, the annealing temperature gradually decreases, the $X$ also gradually decreases, and the worse solution of current that the algorithm can accept gradually becomes larger, so the operating point of the system gradually approaches the maximum current (maximum power) operating point.

At stage 3, after the temperature is gradually reduced until the algorithm accepts only the better perturbation with a higher input current than the reference, the input power steadily converges to the maximum current point (maximum power).

By controlling the slow decay of temperature, the algorithm realizes the search for the global maximum point of power and maximizes the VA utilization of the WPT system.

## V. EXPERIMENTS AND DISCUSSION
### A. VERIFICATION OF VALIDITY OF THE SA METHOD
In order to verify the validity of the proposed SA method for WPT maximum power point tracking, the time domain waveforms are captured at different stages of the control process, which are then compared with the convergence process of the SA method. The half-bridge inverter output voltage and DC bus current waveforms of different stages are given in figure 12- figure 14.

As shown in figure 12, the algorithm achieves the first local maximum power at a DC current amplitude of 650 mA while still accepting lower current as a reference point. This corresponds to the stage 1 of the SA algorithm in figure 11. The annealing temperature is at a higher level, and lower power than the reference point is also acceptable.
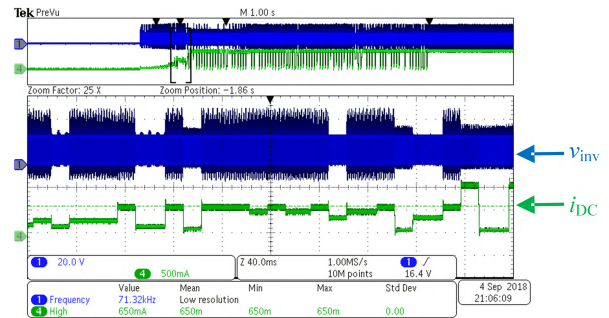


**FIGURE 12.** Half-bridge inverter voltage and DC bus current waveforms when $R_{AC}$ =5 Ω. At stage 1, PWM frequency average = 71.32 kHz (PWM period average = 14.02 µs), DC current amplitude = 650 mA.
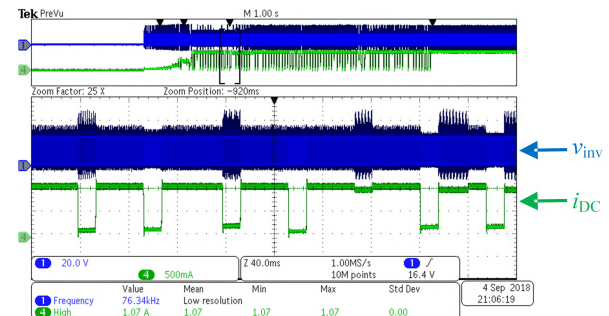


**FIGURE 13.** Half-bridge inverter voltage and DC bus current waveforms when $R_{AC}$ =5 Ω. At stage 2, PWM frequency average = 76.34 kHz (PWM period average = 13.10 µs), DC current amplitude = 1.07 A.
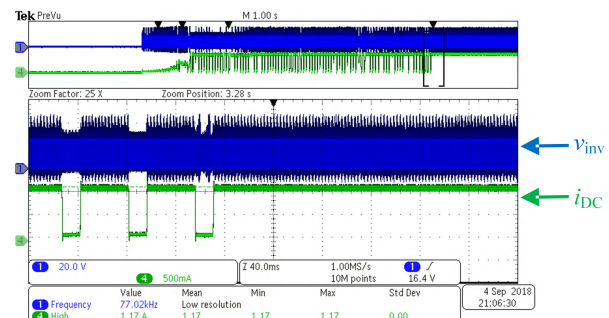


**FIGURE 14.** Half-bridge inverter voltage and DC bus current waveforms when $R_{AC}$ =5 Ω. At stage 3, PWM frequency average = 77.02 kHz (PWM period average = 12.98 µs), DC current amplitude = 1.17 A.

At stage 2 of figure 11, the temperature gradually decreases, at which point the algorithm searches for the global maximum power and perturbs around the global maximum. As shown in figure 13, the DC current amplitude is 1.07A, at which point the acceptance probability $X$ of the worse solution is reduced, and the algorithm begins to converge.

At stage 3 of figure 11, the temperature gradually decreases to a minimum. The algorithm no longer accepts lower power and converges to the global maximum power. In figure 14, the system operates at a PWM frequency of 77.02 kHz, and the DC current reaches a maximum of 1.17 A.

It can be seen from figure 12 - figure 14 that the SA method can effectively converge to the DC current amplitude of 1.17 A after adjusting the working frequency, and then achieve the maximum power point tracking. Experiments have shown that the SA algorithm is valid.

## B. OPTIMIZATION OF TEMPERATURE DECAY SCALE

The critical point of the simulated annealing algorithm is to control the annealing temperature's decay progress. In this paper, the temperature decay process formula is shown in (8).

In order to verify the influence of the decay scale $\alpha$ on the convergence result, a series of experiments were carried out on decay scale $\alpha$ of 0.75 - 0.95. 100 SA processes were carried out under each $\alpha$, and the convergence probability of the system and the average number of iterations required for convergence were counted.

As shown in figure 15, the convergence probability of the algorithm is improved with the increase of the $\alpha$.
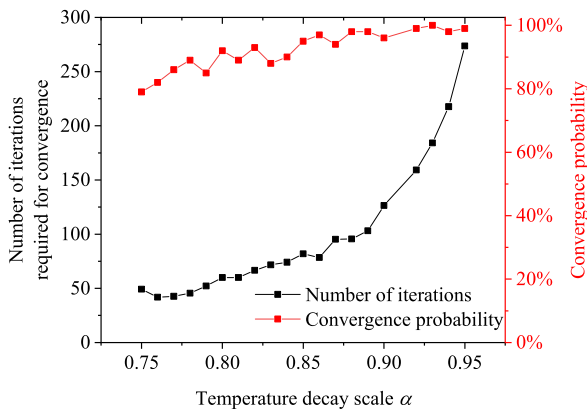


**FIGURE 15.** Average iterations required and convergence probability with increasing $\alpha$ when $R_{AC}$ =15 Ω.

When $\alpha > 0.92$ is reached, the probability of convergence reaches more than 98%. On the other hand, the number of iterations required for the convergence shows an exponential growth with the increase of $\alpha$, which means that an exponential grade of iterations is required to achieve better convergence performance. Therefore, a trade-off between the convergence of the algorithm and the number of iterations is required. In this paper, the optimal $\alpha = 0.80$ is determined based on the iterative convergence probability higher than 90%. At this point, the convergence iterations of 60 are needed in average, and the algorithm can quickly converge to the global maximum power.

## C. SYSTEM LOAD CHANGES

To examine the MPPT performance of the system under different loads, we tested the convergence of the SA control method under stable DC voltage and different loads in this section. The input current characteristic curves of the system under different loads are shown in figure 16. It can be seen that the input current characteristic of the system has significantly changed with the decrease of the load resistance. One current maximum (power maximum) point gradually splits into two. There is a global maximum of current around the PWM signal period 13 $\mu$s and a local maximum of current around the period 8.5 $\mu$s.
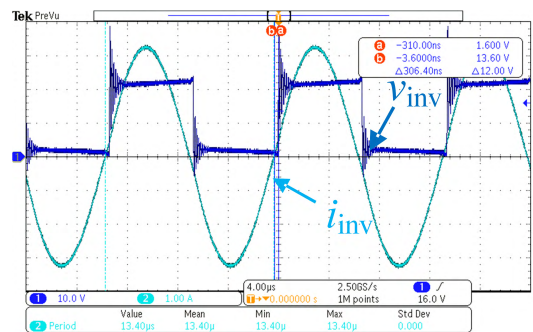
For load resistance ranging from 5 Ω to 30 Ω, the $\alpha$ of 0.80 obtained in the previous section is used for the
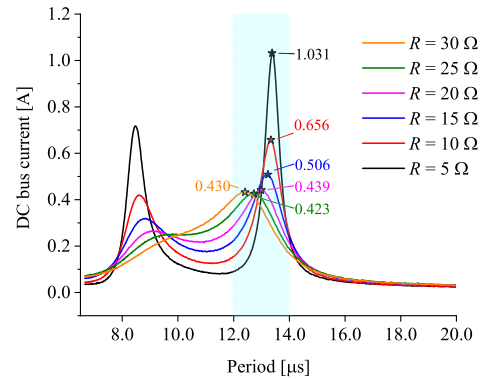


**FIGURE 16.** Input current characteristics under different load conditions.
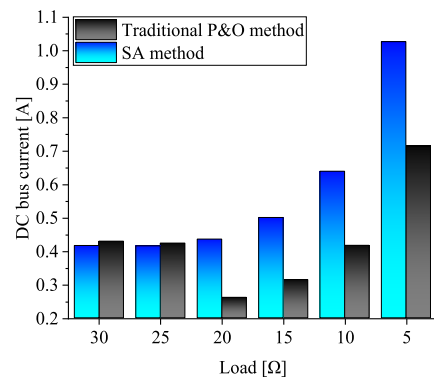


**FIGURE 17.** The comparison of convergence endpoint between the SA method and the P&O method.



**FIGURE 18.** System inverter input waveforms, PWM period = 13.40 $\mu$s (PWM frequency = 74.62 kHz), zero-crossing difference = 306.40 ns (phase difference = 0.14 rad) when $R_{AC}$ = 5 Ω.

SA method control. The convergence endpoint of the SA method is compared with that of the traditional P&O method, as shown in figure 17.

The convergence results of the two methods in the case of bifurcation-free ($R = 25$ Ω, 30 Ω) are basically the same; in the case of bifurcation ($R = 5$ Ω $− 20$ Ω) the SA method is still able to converge to the global maximum power point, and the endpoint power of the SA method is 43% higher than that of the traditional method.

The input power and the input power factor of the system in the steady state are shown in figure 18 and figure 19 after the SA method is finally selected. It can be seen that the application of the SA method can make the system always keep the maximum power transmission close to the unity power factor.
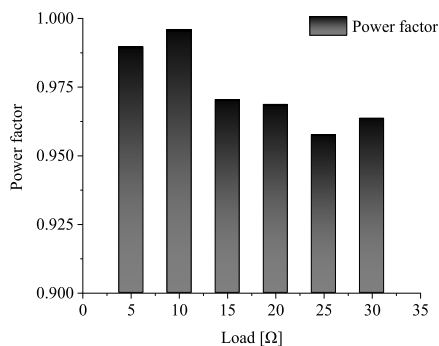
**FIGURE 19.** Power factor results under different load conditions.

It is proved that the maximum power transmission condition and the unity power factor condition can be reached at the same inverter operating frequency.

## VI. CONCLUSION

This paper combines the idea of the SA algorithm and variable frequency control to achieve the global maximum power point tracking (MPPT) of a wireless power transfer system. The proposed SA method solves the problem that the variable frequency MPPT control method will lose the control stability under the condition of bifurcation. And it also makes full use of the inverter's VA capacity, approaching a unity power factor.

Compared with the traditional variable frequency MPPT control method in a WPT system, the results show that the SA method is significantly less affected by the local maximum power and the initial value of the algorithm. It can converge to the global maximum power under different WPT bifurcation conditions, and it can achieve a faster convergence process by controlling the rate of temperature decay while ensuring the convergence.

## REFERENCES

[1] D. H. Tran, V. B. Vu, and W. Choi, "Design of a high-efficiency wireless power transfer system with intermediate coils for the on-board chargers of electric vehicles," *IEEE Trans. Power Electron.*, vol. 33, no. 1, pp. 175–187, Jan. 2018, doi: 10.1109/TPEL.2017.2662067.

[2] C. Cai *et al.*, "Design and optimization of load-independent magnetic resonant wireless charging system for electric vehicles," *IEEE Access*, vol. 6, pp. 17264–17274, 2018, doi: 10.1109/ACCESS.2018.2810128.

[3] P. Si, A. P. Hu, S. Malpas, and D. Budgett, "A frequency control method for regulating wireless power to implantable devices," *IEEE Trans. Biomed. Circuits Syst.*, vol. 2, no. 1, pp. 22–29, Mar. 2008, doi: 10.1109/TBCAS.2008.918284.

[4] C. Cai *et al.*, "Resonant wireless charging system design for 110 kV high voltage transmission line monitoring equipment," *IEEE Trans. Ind. Electron.*, to be published, doi: 10.1109/TIE.2018.2808904.

[5] T. Campi, S. Cruciani, and M. Feliziani, "Wireless power transfer technology applied to an autonomous electric UAV with a small secondary coil," *Energies*, vol. 11, no. 2, p. 352, 2018, doi: 10.3390/en11020352.

[6] J. Wang, M. Hu, C. Cai, Z. Lin, L. Li, and Z. Fang, "Optimization design of wireless charging system for autonomous robots based on magnetic resonance coupling," *AIP Adv.*, vol. 8, no. 5, p. 055004, 2018, doi: 10.1063/1.5030445.

[7] Z. Huang, S.-C. Wong, and C. K. Tse, "Control design for optimizing efficiency in inductive power transfer systems," *IEEE Trans. Power Electron.*, vol. 33, no. 5, pp. 4523–4534, May 2017.

[8] K. Aditya and S. S. Williamson, "A review of optimal conditions for achieving maximum power output and maximum efficiency for a series–series resonant inductive link," *IEEE Trans. Transport. Electrific.*, vol. 3, no. 2, pp. 303–311, Jun. 2017, doi: 10.1109/TTE.2016.2582559.

[9] E. Gati, G. Kampitsis, and S. Manias, "Variable frequency controller for inductive power transfer in dynamic conditions," *IEEE Trans. Power Electron.*, vol. 32, no. 2, pp. 1684–1696, Feb. 2017, doi: 10.1109/TPEL.2016.2555963.

[10] C. Chen, H. Zhou, Q. Deng, and X. Luo, "Nonlinear modeling and feedback control of WPT system via magnetic resonant coupling considering continuous dynamic tuning," in *Proc. Chin. Autom. Congr. (CAC)*, Oct. 2017, pp. 4203–4208.

[11] Y. Luo, Y. Yang, S. Chen, and X. Wen, "A frequency-tracking and impedance-matching combined system for robust wireless power transfer," *Int. J. Antennas Propag.*, vol. 2017, Jan. 2017, Art. no. 5719835, doi: 10.1155/2017/5719835.

[12] N. Liu and T. G. Habetler, "Design of a universal inductive charger for multiple electric vehicle models," *IEEE Trans. Power Electron.*, vol. 30, no. 11, pp. 6378–6390, Nov. 2015, doi: 10.1109/TPEL.2015.2394734.

[13] C.-S. Wang, G. A. Covic, and O. H. Stielau, "Power transfer capability and bifurcation phenomena of loosely coupled inductive power transfer systems," *IEEE Trans. Ind. Electron.*, vol. 51, no. 1, pp. 148–157, Feb. 2004, doi: 10.1109/TIE.2003.822038.

[14] M. Ibrahim *et al.*, "Inductive charger for electric vehicle: Advanced modeling and interoperability analysis," *IEEE Trans. Power Electron.*, vol. 31, no. 12, pp. 8096–8114, Dec. 2016, doi: 10.1109/TPEL.2016.2516344.

[15] S. Q. Liu, J. P. Tan, S. H. Xue, and X. Wen, "Analysis on coupling mechanism characteristics of multi-load wireless power transmission system," *Autom. Electr. Power Syst.*, vol. 40, no. 18, pp. 84–90, 2016, doi: 10.7500/AEPS20160104001.

[16] A. P. Sample, D. T. Meyer, and J. R. Smith, "Analysis, experimental results, and range adaptation of magnetically coupled resonators for wireless power transfer," *IEEE Trans. Ind. Electron.*, vol. 58, no. 2, pp. 544–554, Feb. 2011, doi: 10.1109/TIE.2010.2046002.

[17] N. Shinohara, "Power without wires," *IEEE Microw. Mag.*, vol. 12, no. 7, pp. S64–S73, Dec. 2011, doi: 10.1109/MMM.2011.942732.

[18] M. Pinuela, D. C. Yates, S. Lucyszyn, and P. D. Mitcheson, "Maximizing DC-to-load efficiency for inductive power transfer," *IEEE Trans. Power Electron.*, vol. 28, no. 5, pp. 2437–2447, May 2013, doi: 10.1109/TPEL.2012.2215887.

[19] R. Bosshard, J. Mühlethaler, J. W. Kolar, and I. Stevanović, "Optimized magnetic design for inductive power transfer coils," in *Proc. 28th Annu. IEEE Appl. Power Electron. Conf. Expo. (APEC)*, Mar. 2013, pp. 1812–1819, doi: 10.1109/APEC.2013.6520541.

[20] M. H. Ameri, A. Y. Varjani, and M. Mohamadian, "A new maximum inductive power transmission capacity tracking method," *J. Power Electron.*, vol. 16, no. 6, pp. 2201–2211, 2016, doi: 10.6113/JPE.2016.16.6.2202.

[21] Y. A. Katsigiannis, P. S. Georgilakis, and E. S. Karapidakis, "Hybrid simulated annealing–tabu search method for optimal sizing of autonomous power systems with renewables," *IEEE Trans. Sustain. Energy*, vol. 3, no. 3, pp. 330–338, Jul. 2012, doi: 10.1109/TSTE.2012.2184840.

[22] T. Sutthibun and P. Bhasaputra, "Multi-objective optimal distributed generation placement using simulated annealing," in *Proc. ECTI Int. Conf. Elect. Eng./Electron. Comput. Telecommun. Inf. Technol. (ECTI-CON)*, May 2010, pp. 810–813.

[23] V. E. Jeba, S. Ravichandran, and R. P. K. Devi, "Optimal control of grid connected variable speed wind energy conversion system," in *Proc. Int. Conf. Energy Efficient Technol. Sustainability (ICEETS)*, Apr. 2013, pp. 393–399.

[24] M. A. Azam, S. Abdullah-Al-Nahid, M. A. Kabir, and, S. M. H. Chowdhury, "Microcontroller based maximum power tracking of PV using stimulated annealing algorithm," in *Proc. Int. Conf. Inform., Electron. Vis. (ICIEV)*, May 2012, pp. 298–303.

[25] J. Ohtsubo and K. Nakajima, "Image recovery by simulated annealing with known Fourier modulus," *Opt. Commun.*, vol. 86, nos. 3–4, pp. 265–270, 1991, doi: 10.1016/0030-4018(91)90003-V.

[26] K. P. Wong and C. C. Fung, "Simulated annealing based economic dispatch algorithm," *IEE Proc. C Gener., Transmiss. Distrib.*, vol. 140, no. 6, pp. 509–515, Nov. 1993.

[27] S. Lyden and M. E. Haque, "A simulated annealing global maximum power point tracking approach for PV modules under partial shading conditions," *IEEE Trans. Power Electron.*, vol. 31, no. 6, pp. 4171–4181, Jun. 2016, doi: 10.1109/TPEL.2015.2468592.

[28] Y. Yang, F. Liu, and X. Chen, "A maximum power point tracking control scheme for magnetically coupled resonant wireless power transfer system by cascading SEPIC converter at the receiving side," in *Proc. 32nd Annu. IEEE Appl. Power Electron. Conf. Expo. (APEC)*, Mar. 2017, pp. 3702–3707.

**ZHONGZHENG LIN** was born in Fujian, China, in 1993. He received the B.S. degree in electrical engineering from Wuhan University, China, in 2017, where he is currently pursuing the M.S. degree in electrical engineering with the School of Electrical Engineering.

His current research interests include wireless power transmission technology, and electric power electronics, the research domain involves the magnetic resonance coupling theory and the application research, and the UAV dynamic charging technology research.

**MEILIN HU** was born in Hubei, China, in 1994. She received the bachelor's degree in electrical engineering from Wuhan University, Wuhan, China, in 2016, where she is currently pursuing the master's degree.

Her main research interests include optimization and the design of wireless power transmission system based on resonant magnetic coupling, electromagnetic environment, and security evaluation for wireless charging.

**JUNHUA WANG** was born in Shandong, China, in 1981. He received the Ph.D. degree from The Hong Kong Polytechnic University, Hong Kong, in 2012. He is currently a Professor with the School of Electrical Engineering, Wuhan University.

He joined Carnegie Mellon University as a Post-Doctoral Researcher in 2012 and then was a Research Fellow with the GATE Center for Electric Drive Transportation, MI, USA.

His main research interests include wireless transmission technology based on magnetic resonance, applied electromagnetics, and system equipment for power transmission and distribution.

**CHANGSONG CAI** was born in Henan, China, in 1992. He received the B.Sc. degree in electrical engineering from Tianjin Polytechnic University, Tianjin, China, in 2014, and the M.Eng. degree in electrical engineering from Wuhan University, Wuhan, China, in 2017, where he is currently pursuing the Ph.D. degree, all in electrical engineering.

His main research interests include wireless transmission technology based on magnetic resonance and applied electromagnetics.

**ZHIJIAN FANG** received the B.S. and Ph.D. degrees in electrical engineering and automation from the Huazhong University of Science and Technology, Wuhan, China, in 2010 and 2015, respectively.

From 2016 to 2017, he was a Post-Doctoral Research Fellow with the Department of Electrical and Computer Engineering, Ryerson University, Toronto, Canada. Since 2015, he has been a Post-Doctoral Research Fellow with the School of Electrical Engineering, Wuhan University, Wuhan.

His research interests include high performance DC/DC converter, battery charger, and renewable energy applications.

**JUNKUN ZHANG** was born in Hubei, China, in 1992. He received the B.S. degree in electrical engineering from Hubei Polytechnic University, Huangshi, China, in 2014, and the M.S. degree in electrical engineering from Wuhan University of Technology, Wuhan, China, in 2017. In 2017, he joined the Institute of New Energy, Wuhan, where he is currently a Technique Supporting Executive.

He is currently pursuing the Ph.D. degree with Hunan University, Changsha, China. His research interests include inductive power transfer technology and dc/dc converters.

• • •